



Multi-objective materials bayesian optimization with active learning of design constraints: Design of ductile refractory multi-principal-element alloys

Danial Khatamsaz^a, Brent Vela^{b,*}, Prashant Singh^{b,c}, Duane D. Johnson^{c,d}, Douglas Allaire^a, Raymundo Arróyave^{a,b,e}

^a J. Mike Walker '66 Department of Mechanical Engineering, Texas A&M University, College Station, TX 77843, USA

^b Department of Materials Science and Engineering, Texas A&M University, College Station, TX 77843, USA

^c Ames Laboratory, U.S. Department of Energy, Iowa State University, Ames, IA 50011, USA

^d Department of Materials Science & Engineering, Iowa State University, Ames, IA 50011, USA

^e Department of Industrial and Systems Engineering, Texas A&M University, College Station, TX 77843, USA

ARTICLE INFO

Article history:

Received 20 March 2022

Revised 3 June 2022

Accepted 27 June 2022

Available online 29 June 2022

Keywords:

Bayesian optimization

Active learning

ICME

DFT

Refractory multi-principal element alloys

ABSTRACT

Bayesian Optimization (BO) has emerged as a powerful framework to efficiently explore and exploit materials design spaces. To date, most BO approaches to materials design have focused on the materials discovery problem as if it were a single expensive-to-query 'black box' in which the target is to optimize a single objective (i.e., material property or performance metric). Also, such approaches tend to be constraint agnostic. Here, we present a novel multi-information BO framework capable of actively learning materials design as a multiple objectives and constraints problem. We demonstrate this framework by optimally exploring a Refractory Multi-Principal-Element Alloy (MPEA) space, here specifically, the system Mo-Nb-Ti-V-W. The MPEAs are explored to optimize two density-functional theory (DFT) derived ductility indicators (Pugh's Ratio and Cauchy pressure) while learning design constraints relevant to the manufacturing of high-temperature gas-turbine components. Alloys in the BO Pareto-front are analyzed using DFT to gain an insight into fundamental atomic and electronic underpinning for their superior performance, as evaluated within this framework.

© 2022 Acta Materialia Inc. Published by Elsevier Ltd. All rights reserved.

1. Introduction

1.1. Motivation

Improved gas-turbine engine (GTE) technology requires the continued development of high-temperature materials with higher strength and creep resistance at operational temperatures. The current materials of choice for use in such extreme operating conditions are Ni-based superalloys [1]. As gas-turbine efficiency can be improved by increasing the inlet temperature to the engine [2], there is a motivation to operate gas turbine engines at increasingly elevated temperatures. Currently, Ni-based superalloys operate at temperatures approaching their melting temperatures ($\sim 0.9 T_m$) [3]. Novel gas turbine technologies require metallic materials that can perform at temperatures exceeding 1150 °C, beyond

which nickel-based superalloys are unable to perform due to inherent limitations from their melting temperatures [1]. While sophisticated cooling systems, such as cooling channels [4], thermal barrier coatings [5], and engineering of thermal conductivity [5], have been employed in the design of modern jet turbine blades, Ni-based superalloys are quickly approaching their operational limit, spurring exploration for novel, ultrahigh-temperature materials.

Recently, refractory multi-principal-element alloys (MPEAs) have garnered much attention as an emerging class of high-temperature materials. MPEAs consist of several alloying components (typically 4 or more) with concentrations ranging from 5 to 35 at.%, whereas conventional alloys rely on a single predominant constituent. Refractory MPEAs generally form body-centered-cubic (bcc) solid solutions [6] that have been shown to possess high-temperature properties comparable to those of the current Ni-based superalloys [7]. The compositional complexity of these refractory MPEAs creates opportunities to design alloys with unique properties, such as high-temperature yield strength [7], low density [8], creep resistance [9], and oxidation resistance [10]. How-

* Corresponding author.

E-mail address: brentvela@tamu.edu (B. Vela).

ever, while refractory MPEAs may satisfy performance constraints at elevated temperatures, due to the ductile-to-brittle-transition temperature of these alloys, many are brittle at room temperature and thus not machinable. The extreme difficulty associated with processing refractory alloys has historically limited their development [11]. In fact, room temperature ductility is a significant bottleneck in the development of refractory MPEAs [12]. For this reason we proposed a novel framework capable of multi-objective Bayesian optimization and active learning of multiple constraint boundaries in order to optimize for ductility in refractory MPEAs while under GTE relevant design constraints.

With the advent of Integrated Computational Materials Engineering (ICME), it has become possible solve the inverse problem and design alloys with tailored properties [13]. ICME relies on simulation in tandem with experiments to build linkages along the process-structure-property performance (PSPP) chain. Performance constraints are often defined in terms of materials properties. In turn, these materials properties are dictated by the structure of the material. Finally, the structure of the material is determined by the processing conditions used to realize the material. When inverted, these linkages can guide the search for alloys that meet certain performance constraints. Thus within an ICME framework, refractory MPEAs can be designed, in principle, with ductility in mind.

Other works where Bayesian optimization is used within the ICME paradigm include examples of multi-objective optimization, optimization under unknown constraints, and active learning to reduce the design space. Regarding multi-objective optimization, Solomou et al. [14] demonstrated tri-objective Bayesian optimization for the design of precipitation hardened shape memory alloys, simultaneously optimizing for austenitic finish temperature, specific thermal hysteresis (defined by the difference of austenitic finish temperature and martensitic start temperature), and the maximum transformation strain. Regarding Bayesian optimization under constraints, Griffiths et al. [15] were able to optimize drug-like molecules while under the constraint that said molecules must be valid molecular structures. The Bayesian optimization was performed over the latent space of a variational autoencoder that encoded the molecular structure of candidate designs. The authors used Bayesian Neural Network (BNN) classifiers that would output the probability of a point in the latent space being mapped to a valid molecular structure or not. Optimization was then carried out in feasible regions of the design space. Regarding active learning to reduce the design space, using the e-PAL framework, Jablonka et al. [16] were able to use active learning to efficiently estimate the Pareto-front during the multi-objective design of polymers for dispersant applications. The polymers were designed for optimal adsorption free energy, dimer free energy barrier, and radius of gyration. The polymer design space was iteratively reduced as e-PAL classified points as either likely dominated or likely Pareto optimal, actively learning the Pareto-front. The framework converges when all remaining points are classified as dominated (disregarded) or Pareto optimal.

In this work, we present a novel framework to perform multi-objective Bayesian optimization under unknown constraints. The framework is capable of actively learning the constraint boundaries as well as iteratively reducing the design space by discerning between feasible and infeasible design regions. We seek to computationally link structure to property in refractory MPEAs by optimizing well-known ductility indicators, i.e., Pugh's ratio and Cauchy's pressure. The framework is benchmarked by designing ductile refractory MPEAs while under two constraints (density and solidus temperature) relevant to gas turbine application as a case study. Furthermore, a detailed DFT calculations is done on predicted MPEAs to assess underlying features driving ductility and its origin. While this work is limited to ductility, there exists opportunity to account for more objectives and constraints.

1.2. Design objectives and constraints

A known ductility indicator in refractory MPEA design is the valence electron concentration (VEC), as shown to be true theoretically [17] and experimentally [12]. A low VEC will promote shear failure and suppress cleavage failure in bcc-based alloys due to shear instability introduced by decreasing VEC [17]. It is a common MPEA design rule that that refractory alloys with low VECs are more ductile than those with higher VECs. For example, driven by the fact that equimolar HfNbTiZr and HfNbTaTiZr alloys are known to be ductile, Sheikh et al. [12] minimized the VEC in the HfNbTaTiZr alloy space under the constraint that the alloy be single-phase bcc. This constraint was encoded by the enthalpy of mixing and the atomic size mismatch, which are known indicators of the stability of the bcc solid-solution phase. The authors identified and synthesized $\text{Hf}_{0.5}\text{Nb}_{0.5}\text{Ta}_{0.5}\text{Ti}_{1.5}\text{Zr}$ which had an elongation at fracture of 18.8%. While the VEC is useful in identifying ductile alloys in a HTP manner, it does not *explicitly* account for elasticity in the crystal structure of the alloy. This points toward the inability of such metrics to find the *most* ductile alloys, therefore, indicators that capture the crystalline elasticity of an alloy are needed.

The ductility/brittleness of MPEAs can also be encoded by metrics derived from the elastic properties of alloys, such as the Pugh's ratio and the Cauchy pressure. These two indicators of ductility have been used extensively in the design of ductile MPEAs [18–20]. For pure crystalline metals, the Pugh's ratio is defined as the ratio of the bulk modulus over the shear modulus (B/G). This ratio encodes the competition between resistance to plastic deformation (G) and the fracture strength (B); Thus B/G captures the extent of the plastic range without fracture [21]. Pettifor [22] proposed Cauchy pressure as an indicator of intrinsic ductility/brittleness, which is the difference of two elastic constants C_{12} and C_{44} . A positive Cauchy pressure indicates non-directional metallic bonds resulting in intrinsic ductility of the crystal, whereas a negative Cauchy pressure corresponds to directional bonds and results in an intrinsically brittle crystal structure. Both indicators can be estimated with high-fidelity DFT frameworks at great computational cost. However, as the MPEA composition space is combinatorially vast, sufficient exploration of the space is intractable using conventional (computational or experimental) approaches.

Furthermore, while a given alloy may be ductile, its other properties may not be appropriate for GTE applications. For example, a ductile alloy may be too dense ($\rho < 11$ g/cc) for use in aviation. Likewise, an alloy that is optimized for ductility may have too low of a solidus temperature ($T_s < 2000$ °C) for use inside the hot-zones of GTEs. While we do not wish to optimize for these two properties, we still must classify alloys based on whether they meet said constraints. Therefore, to explore effectively this vast design space for ductile alloys while under design constraints related to GTE application, and under resource constraints due to the high cost of the DFT truth-model, intelligent optimization schemes capable of balancing resources between optimization and classification are needed. This classification step essentially aims to discover the feasible alloy space amenable for further optimization.

1.3. Multi-information source, constraint-aware bayesian optimization

Limitations on computational resources is a bottleneck in solving optimization problems in engineering applications. Many of engineering systems are in the form of black-box objective functions that require numerical approaches to search the input space for designs corresponding to optimum values of the quantities of interest. Among the proposed approaches for such design applications are Bayesian optimization (BO) techniques. Bayesian techniques offer a more efficient optimization by employing a heuristic-based

search and, more importantly, the ability to update the system's state of knowledge continuously as new observations are introduced to the system.

Furthermore, in many instances in materials engineering, several models are available that represent the same system of interest. These models are based on different assumptions and/or simplifications, and thus differ in fidelity and cost of evaluation. These models are treated as sources that provide useful information about a quantity of interest and are thus called *information sources*. In Refs. [23–27], it has been shown that employing multi-information sources in multi-fidelity BO frameworks offers a more robust and efficient approach to implement in design applications in comparison to single model optimization techniques.

In multi-information source BO, the assumption is that every source contains useful information regarding optimum design; thus, accurately fusing these sources results in a fused model that can mimic the response of the highest-fidelity model, known as the ground truth, enabling the search of the design space for the optimum design at no considerable computational cost. As later developments of the works [23–27], in Ref. [28], a novel framework is proposed that is capable of optimizing multiple objectives in multi-fidelity settings. In many engineering applications, there are several quantities of interest to be optimized simultaneously that urges the need for multi-objective optimization techniques. In Ref. [28], it has been shown that single fidelity approaches either using a BO framework or other techniques such as ParEGO and genetic algorithms are outperformed computationally when multiple sources of information contribute to provide information about the quantities of interest.

Regarding classification (or identification of a materials feasible space), a challenge in constrained optimization problems is correctly recognizing the feasible regions and their boundaries. Although sometimes checking the feasibility of a design input is done at no considerable costs, for example, by simply inserting the design variables into an analytical equation, there exist cases that constraints are defined by computationally expensive models which makes it impractical to verify the feasibility of every single design by querying their respective models. Therefore, constructing cheaper machine learning models to represent the constraints can reduce the overall cost of solving a constrained optimization problem.

A natural choice is to use surrogate models and information-theoretic approaches to learn the constraint models and accurately estimate their value at different locations in the input space [29]. However, it might be unnecessary to model the constraint over the entire input space as the boundary separating the feasible and infeasible regions is what is truly of importance. Thus, in this study, we propose a Bayesian classification (BC) framework that uses classifiers and an active learning technique to effectively learn the constraint boundaries and recognize the feasible regions via checking the class memberships of any locations in the input space. Similar to multi-fidelity BO frameworks, in classification problems, there may exist several information sources that model the same constraint. Thus, we introduce our classification framework in form of a multi-fidelity BC configuration. Then, by coupling this multi-fidelity BC framework with the multi-objective multi-fidelity Bayesian framework introduced in Khatamsaz et al. [28], we create a design framework that actively learns the constraint boundaries and guides the search toward the optimum design by recognizing the feasible regions.

Here, we make further developments to the multi-objective, multi-fidelity BO framework introduced in Ref. [28] and propose a novel approach to solve constrained-design problems. Specifically, we deploy this framework in the Mo-Nb-Ti-V-W system, an exemplary MPEA system. By balancing the need to learn the constraint boundaries more accurately with improving the system's knowl-

edge about the optimum values of quantities of interest, our proposed framework is able to make decisions about the best action to take at every stage of the process.

2. Methods

2.1. Gaussian process regression

In the context of BO, surrogate models are employed to model the behavior of objective functions and to represent a cheaper source to estimate the objective values associated to different design inputs and then calculate the expected gains regarding a potential design evaluation at much lower computational costs without the need to call the objective function directly.

We have implemented Gaussian process regression (GPR) to model objective functions [30]. Gaussian process models are powerful tools for probabilistic modeling purposes. They are easy to manipulate and simple to update as new observations are made available. In multi-fidelity BO frameworks, there are several sources to estimate the same quantity of interest at different fidelity levels, each providing key piece of information about the ground-truth quantity of interest. In presence of multi-information sources, several Gaussian processes are constructed to represent the response surface of these information sources.

Following Refs. [26,27], we assume we have available some set of information sources, $f_i(\mathbf{x})$, where $i \in \{1, 2, \dots, S\}$, that can be used to estimate the quantity of interest, $f(\mathbf{x})$, at design point \mathbf{x} . These surrogates are indicated by $f_{GP,i}(\mathbf{x})$. Assuming there are N_i evaluations of information source i denoted by $\{\mathbf{X}_{N_i}, \mathbf{y}_{N_i}\}$, where $\mathbf{X}_{N_i} = (\mathbf{x}_{1,i}, \dots, \mathbf{x}_{N_i,i})$ represents the N_i input samples to information source i and $\mathbf{y}_{N_i} = (f_i(\mathbf{x}_{1,i}), \dots, f_i(\mathbf{x}_{N_i,i}))$ represents the corresponding outputs from information source i , then the posterior distribution of information source i at design point \mathbf{x} is given as

$$f_{GP,i}(\mathbf{x}) | \mathbf{X}_{N_i}, \mathbf{y}_{N_i} \sim \mathcal{N}(\mu_i(\mathbf{x}), \sigma_{GP,i}^2(\mathbf{x})) \quad (1)$$

where

$$\begin{aligned} \mu_i(\mathbf{x}) &= K_i(\mathbf{X}_{N_i}, \mathbf{x})^T [K_i(\mathbf{X}_{N_i}, \mathbf{X}_{N_i}) + \sigma_{n,i}^2 I]^{-1} \mathbf{y}_{N_i} \\ \sigma_{GP,i}^2(\mathbf{x}) &= k_i(\mathbf{x}, \mathbf{x}) - K_i(\mathbf{X}_{N_i}, \mathbf{x})^T \\ &\quad [K_i(\mathbf{X}_{N_i}, \mathbf{X}_{N_i}) + \sigma_{n,i}^2 I]^{-1} K_i(\mathbf{X}_{N_i}, \mathbf{x}) \end{aligned} \quad (2)$$

where k_i is a real-valued kernel function over the input space, $K_i(\mathbf{X}_{N_i}, \mathbf{X}_{N_i})$ is the $N_i \times N_i$ matrix whose m, n entry is $k_i(\mathbf{x}_{m,i}, \mathbf{x}_{n,i})$, and $K_i(\mathbf{X}_{N_i}, \mathbf{x})$ is the $N_i \times 1$ vector whose m th entry is $k_i(\mathbf{x}_{m,i}, \mathbf{x})$ for information source i . We have also included the term $\sigma_{n,i}^2$, which is used to model observation error for information sources based on experiments. Without loss of generality, we employ the squared exponential covariance function as the kernel function specified as

$$k_i(\mathbf{x}, \mathbf{x}') = \sigma_s^2 \exp \left(- \sum_{h=1}^d \frac{(\mathbf{x}_h - \mathbf{x}'_h)^2}{2l_h^2} \right) \quad (3)$$

where d is the dimensionality of the input space, σ_s^2 is the signal variance, and l_h , where $h = 1, 2, \dots, d$, is the characteristic length-scale that indicates the correlation strength between the points within the dimension h . The parameters σ_s^2 and l_h associated with each information source can be estimated by maximizing the log marginal likelihood.

When using multiple information sources to estimate a ground truth quantity of interest, it is important to quantify the uncertainty in the response of the information sources with respect to the ground truth, which is defined as the discrepancy term to compensate for the lower fidelity estimation of the ground truth quantity of interest. We quantify the total variance that captures both the variance associated with the Gaussian process representation

and the quantified variance associated with the fidelity of the information source over the input space, as

$$\sigma_i^2(\mathbf{x}) = \sigma_{GP,i}^2(\mathbf{x}) + \sigma_{f,i}^2(\mathbf{x}) \quad (4)$$

where $\sigma_{f,i}^2(\mathbf{x})$ is the variance related to the fidelity of information source i that can be estimated from, for example, expert opinion or available real-world data.

2.2. Gaussian process classification

Similar to optimization problems, Bayes' theorem can be employed to calculate the joint probability $p(y|\mathbf{x})$, where y is the class label, in classification problems:

$$p(y|\mathbf{x}) = \frac{p(y)p(\mathbf{x}|y)}{\sum_{c=1}^C p(C_c)p(\mathbf{x}|C_c)} \quad (5)$$

A challenge of Gaussian process classification (GPC) that is not present in Gaussian process regression is that of non-Gaussian likelihoods in GPC. To overcome this, following Ref. [30], we use a discriminative GPC approach that seeks to model $p(y|\mathbf{x})$ directly, which avoids the need to specify prior distributions over $p(y)$ and the specification of class-conditional densities, $p(\mathbf{x}|C_c)$. Discriminative GPCs are probabilistic classifiers that predict the probability of belonging to a class by placing a Gaussian process prior over a latent function $f(\mathbf{x})$ and computing the posterior distribution at a desired location \mathbf{x} [30,31]. Here, we are not interested in the values of the latent function, but it is used to conveniently formulate the classifier. This latent function is responsible to connect the input to the output, where the output is class membership probability. Consequently, we need the latent function posterior distribution respectively. The Laplace approximation algorithm is employed that utilizes Gaussian approximation to the posterior of the latent variables. The approximated posterior is then used to obtain the class membership distribution, where Monte Carlo sampling is done to estimate the class membership probability. Similar to the construction of Gaussian process regressions, assuming we have available some set of information sources $i \in \{1, 2, \dots, S\}$ with N_i labeled samples, the latent function $f_i(\mathbf{x})$ has a multivariate normal distribution defined by

$$\begin{aligned} \mu_i(\mathbf{x}) &= K_i(\mathbf{X}_{N_i}, \mathbf{x})^T [K_i(\mathbf{X}_{N_i}, \mathbf{X}_{N_i})]^{-1} f(\mathbf{X}) \\ \Sigma_i(\mathbf{x}) &= k_i(\mathbf{x}, \mathbf{x}) - K_i(\mathbf{X}_{N_i}, \mathbf{x})^T \\ &\quad [K_i(\mathbf{X}_{N_i}, \mathbf{X}_{N_i})]^{-1} K_i(\mathbf{X}_{N_i}, \mathbf{x}) \end{aligned} \quad (6)$$

The class label predictions are obtained by sampling from the calculated posterior distribution and passing the samples through a sigmoid function σ , for example, the logistic sigmoid, to ensure the output is bounded to [0,1]. Then the mean of the obtained distribution is the class membership probabilities.

In the context of BC and learning purposes, the uncertainty associated to the predictions are essential in calculation of an expected utility value. Note that this is the distinguishing characteristic of the Gaussian process classification as a probabilistic model in comparison to other classification techniques that makes GPC well-suited for probabilistic frameworks and learning purposes. A more detailed discussion is presented in Rasmussen and Williams [30].

2.3. Information fusion of multiple sources

Assuming that every information source participating in the optimization process contains some useful information regarding the ground truth quantity of interest, the goal is to accurately fuse the information provided by these information sources to approximate the quantity of interest as accurately as possible at much lower

costs in comparison to evaluating the ground truth objective function [26,32–34].

Several approaches exist for fusing multiple sources of information, such as Bayesian modeling averaging [35–40], the use of adjustment factors [41–44], covariance intersection methods [45], and fusion under known correlation [46–48].

Our assumption is that every information source contains useful information regarding the ground truth quantity of interest and as more information sources are incorporated into a fusion process, the expectation is to have the variance of the quantity of interest estimates decreased. This is not necessarily the case for all of the aforementioned fusion techniques with the exception of fusion under known correlation. Unlike most traditional multi-fidelity approaches [49–56], in our approach, we do not assume a hierarchy of information sources and our goal is optimization with respect to ground truth and not optimization with the highest fidelity source. Therefore, determining correlations prior to fusion is essentially important. To estimate the correlation coefficients between information sources, we use the reification process introduced in Refs. [32,34]. In reification process, a pair of information sources are selected each time and they are reified ('made real') in turn, which means one information source is assumed to be the true model and the deviation of the second information source with respect to the reified model is calculated. These calculated deviations are used to obtain the correlation between the mean squared errors of the information sources. The covariance matrix is formed after the reification is done over each pair of information sources. Readers are encouraged to check Refs. [26,32–34] for detailed discussion on how the correlation estimation is performed. In case of known correlations between the discrepancies of information sources, the fused mean and variance at a particular design point \mathbf{x} are defined as Winkler [48]

$$\mathbb{E}[\hat{f}(\mathbf{x})] = \frac{\mathbf{e}^T \tilde{\Sigma}(\mathbf{x})^{-1} \boldsymbol{\mu}(\mathbf{x})}{\mathbf{e}^T \tilde{\Sigma}(\mathbf{x})^{-1} \mathbf{e}} \quad (7)$$

$$\text{Var}(\hat{f}(\mathbf{x})) = \frac{1}{\mathbf{e}^T \tilde{\Sigma}(\mathbf{x})^{-1} \mathbf{e}} \quad (8)$$

where $\mathbf{e} = [1, \dots, 1]^T$ is a S dimensional column vector of ones, $\boldsymbol{\mu}(\mathbf{x}) = [\mu_1(\mathbf{x}), \dots, \mu_S(\mathbf{x})]^T$ given S models, and $\tilde{\Sigma}(\mathbf{x})^{-1}$ is the inverse of the covariance matrix between the information sources. A more detailed discussion on this fusion technique and some examples of its implementation are presented in Refs. [23,25,27,32,57–60].

2.4. Multi-objective optimization

A multi-objective optimization problem can be defined as

$$\text{minimize } \{f_1(\mathbf{x}), \dots, f_n(\mathbf{x})\}, \mathbf{x} \in \mathcal{X} \quad (9)$$

where $f_1(\mathbf{x}), \dots, f_n(\mathbf{x})$ are the objectives and \mathcal{X} is the feasible design space. In multi-objective optimization problems, it is usually the case that there is no single solution that optimizes all objectives simultaneously. Thus, the solution to such design problems is a set of non-dominated designs that are not superior to each other, forming the Pareto-front in the objective space. In this case, optimal solutions, \mathbf{y} , to a multi-objective optimization problem with n objectives are denoted as $\mathbf{y} \prec \mathbf{y}'$, and are defined by

$$\begin{aligned} \{\mathbf{y} : \mathbf{y} = (y_1, y_2, \dots, y_n), y_i \leq y'_i \forall i \in \{1, 2, \dots, n\}, \\ \exists j \in \{1, 2, \dots, n\} : y_j < y'_j\} \end{aligned} \quad (10)$$

where $\mathbf{y}' = (y'_1, y'_2, \dots, y'_n)$ denotes any possible objective output. The set of $\mathbf{y} \in \mathcal{Y}$, where \mathcal{Y} is the objective space, is the Pareto-front of the problem.

There are several techniques to employ to estimate the Pareto-front in multi-objective optimization problems such as weighted

sum approach [61], the adaptive weighted sum approach [62], normal boundary intersection methods [63], hypervolume indicator methods [64–70], and others. In the context of BO, and working with expected improvement-based algorithms, the hypervolume indicator approaches are well-suited as they allow for introducing a single random variable, combining multiple random variables (here, objective values), to consider the uncertainty of all other variables as a whole. Thus, in a BO framework, a hypervolume indicator can be the target variable to be optimized. The idea is to define the volume between the estimated Pareto-front and a fixed point in the objective space as the hypervolume and relate the expected improvement associated to each objective value to the total hypervolume and calculate the expected hypervolume improvement. We follow the work proposed in Refs. [28,71] for BO of multi-objective functions in presence of multiple information sources. An in-depth discussion on the calculation of the expected hypervolume improvement can be found in the mentioned references and [72].

2.5. Active learning in Bayesian classification

Using GPCs to label the samples, there are uncertainty associated to the label predictions that also shows how uncertain is the classifier about the label at a particular location. The class membership \mathbb{Y} is a random variable indicated by a distribution \mathbb{P} . In general, we look for a measure that shows the degree of uncertainty based on the given distribution for class memberships. A convenient option is using discrete entropy to calculate the uncertainty in the label predictions:

$$H(Y) = - \sum_{i=1}^k p_i \log(p_i) \quad (11)$$

where there are k classes and p_i is the probability of belonging to class i . Higher values of entropy shows the larger uncertainty of the classifier about the label of a sample. Thus, we look forward to query samples and update the classifiers at locations where the classifier is highly uncertain about the true label.

An issue when using entropy as a measure of uncertainty is that in the case of multi-class classification, it is possible that the classifier is only uncertain about the memberships in, for example, two classes and is highly certain about the other class memberships that may be unimportant. This is the case when the entropy is still high, and it does not provide any information about the confidence on some class memberships. To address this issue, following Ref. [73], we can take the “Best versus second Best” approach. This technique only considers the top two uncertain class memberships and measures the uncertainty based on the difference between the two probabilities.

For our constrained BO, we only perform binary classification since we are using classifiers to separate the feasible and unfeasible regions. In this case, our problem reduces to finding the samples closest to the classifier's predicted constraint boundary. In other words, the samples with the smallest difference between class membership probabilities are chosen to be queried from the constraints to update the classifier and learn about the true constraint boundary.

2.6. Truth model – density functional theory

The truth model in the multi-objective optimization side framework was queried through the DFT-based KKR (Korringa-Kohn-Rostoker Green's function) method, in which the coherent-potential approximation (CPA) accounts properly for direct configurational average over chemical disorder [74], concomitantly with the charge self-consistency required within the standard DFT. One

of the objectives, i.e., bulk moduli, used by the framework were calculated by employing a gradient-corrected exchange-correlation functional (PBE) [75]. Additionally, the Warren-Cowley short-range order (SRO, given as $\alpha_{\mu\nu}(k; T)$) of the designed compositions were calculated as implemented within DFT-KKR-CPA linear-response theory to analyze the ordering tendencies found in the final compositions [76–78].

The structural optimization to estimate local-lattice distortion (LLD), a ductility metric of designed compositions in Table 1, were performed using the DFT method as implemented within the Vienna Ab initio Simulation Package [75,79–81]. The Perdew–Burke–Ernzerhof (PBE) generalized gradient approximation (GGA) functional [75] was employed for geometrical relaxations with total-energy and force convergence criteria of 10^{-6} eV and 0.01 eV/Å, respectively. To mimic MPEAs within a finite cell, supercells were designed using SCRAPs [82] – SuperCell Random APproximateS. We chose two SCRAP sizes, (i) 128 atoms for design 1, and (ii) 160 atoms for design #2 to #7 in Table 1. The largest possible supercells were used to avoid size effects [83]. The Brillouin zone integration in charge self-consistency and ionic relaxation were performed on $1 \times 1 \times 1$ using Monkhorst–Pack method [84] with a plane-wave cutoff energy of 520 eV, where the effect of the core electrons and interaction between the nuclei and the valence was treated by the projector-augmented wave (PAW) [85,86].

The DFT-KKR-CPA is expensive to query. Therefore, computationally inexpensive alternatives, e.g., rule-of-mixtures approximation, are needed for both the Pugh's ratio and the Cauchy pressure to explore the objective space. In this work, to estimate the Pugh's ratio cheaply, we express the bulk and shear modulus in terms of the Poisson ratio. We then calculate the weighted average of the elemental Poisson ratio to evaluate Eq. (12), where i iterates along all N elements in the design space, ν_i and χ_i is the Poisson ratio of the i th element, respectively. For the Cauchy pressure, we calculate the weighted average of C_{12} and C_{44} elastic constants and find their difference according to Eq. (13).

$$\overline{B/G} = \frac{2(1 + \sum_{i=1}^N \nu_i \chi_i)}{3(1 - \sum_{i=1}^N \nu_i \chi_i)} \quad (12)$$

$$\overline{C}_{pres} = \sum_{i=1}^N C_{12} \chi_i - \sum_{i=1}^N C_{44} \chi_i \quad (13)$$

2.7. Thermodynamic simulation

The truth model in the classification side of the framework was queried through a high fidelity CALculation of PHase Diagrams (CALPHAD) based simulation scheme. Equipped with the MPEA specific TCHEA5 thermodynamic database, Thermo-Calc's equilibrium simulation was used to query both the density and the solidus temperature. The integration of these models within this automated framework was achieved using the Thermo-Calc API, TC-Python. These thermodynamic equilibrium simulations are relatively expensive to query. As such, cheaper alternatives are required to explore the constraint space. The rule-of-mixtures was used as a cheap alternative to the CALPHAD truth model for both density and solidus temperature.

3. Results

3.1. Multi-fidelity Bayesian classification

In this work, we use Gaussian process classification (GPC) to model the constraint boundaries to distinguish the feasible and unfeasible regions in the design space (binary classification). A

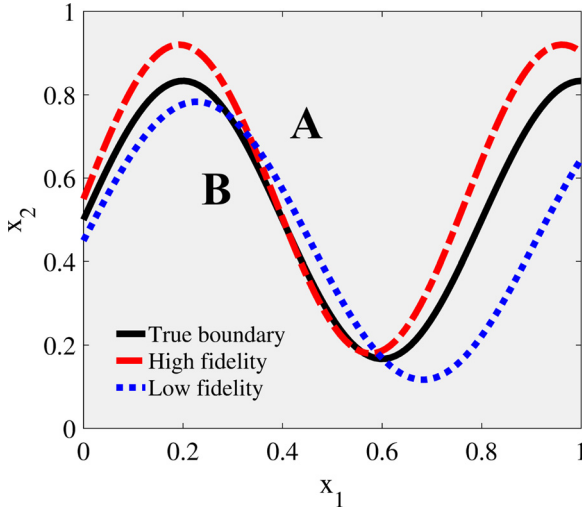


Fig. 1. 2 Dimensional classification test problem. The space is divided into regions 'A' and 'B'. Two lower fidelity models estimate the true boundary.

BC framework employs entropy measure to determine the uncertainty and search for the best next experiment to query the constraints and update corresponding GPCs to decrease the labeling uncertainty the most. Similar to multi-fidelity BO frameworks introduced in Refs. [23,25,26,28], a BC framework can be designed in multi-fidelity settings. There may exist several models to represent the same constraint with different fidelity levels and evaluation costs. Using the reification process followed by fusion of multiple sources introduced in Refs. [32,48,57], a fused classifier can be constructed for each constraint that accurately models the constraint boundary using information gained from different sources. To show how a multi-fidelity BC approach is able to determine the constraint boundaries more accurately and efficiently, a test problem is designed and shown in Fig. 1. The highest fidelity model represents the true boundary while there are also two

lower fidelity models to estimate the boundary between regions 'A' and 'B'.

In Fig. 2, the results of employing the BC framework in single- and multi-fidelity settings have been shown. While the black curve is the true boundary that is desired to be recognized, the blue curve shows the classifier's estimation of the boundary with 95% confidence intervals. Red dots are the locations in the input space queried in the BC process to update the classifiers and decrease the uncertainty of classification. They show the estimated constraint boundary after 20, 50, and 100 queries from the highest fidelity model. After every 10 queries to lower fidelity models, a fused model is constructed and the design closest to the boundary is chosen to be queried from the highest fidelity model. The closer a design is to the estimated boundary, the larger the classifier uncertainty is about its class membership. Note that the boundary is very close to 50% in case of binary classification.

As seen in Fig. 2, employing multiple sources to represent the same constraint has improved the performance of the classifier significantly. Not only it has estimated the true boundary more accurately with narrower confidence intervals, but also it has done so with a smaller number of queries from the highest fidelity model. Plus, the queried locations show how more effectively the framework is able to make highly informative queries to help in determining the constraint boundary.

3.2. Proposed design framework

Fig. 3 illustrates the flowchart of the proposed design framework to solve constrained optimization problems. Here, the BO and BC frameworks are coupled to build a larger configuration that wisely and optimally makes decisions about improving the system's knowledge regarding the optimum design while learning the constraint boundaries to recognize the feasible design region.

In the BO part of this design framework, the most up-to-date fused classifiers are used to determine the feasible regions and prevent the framework to search unfeasible regions. Therefore, be-

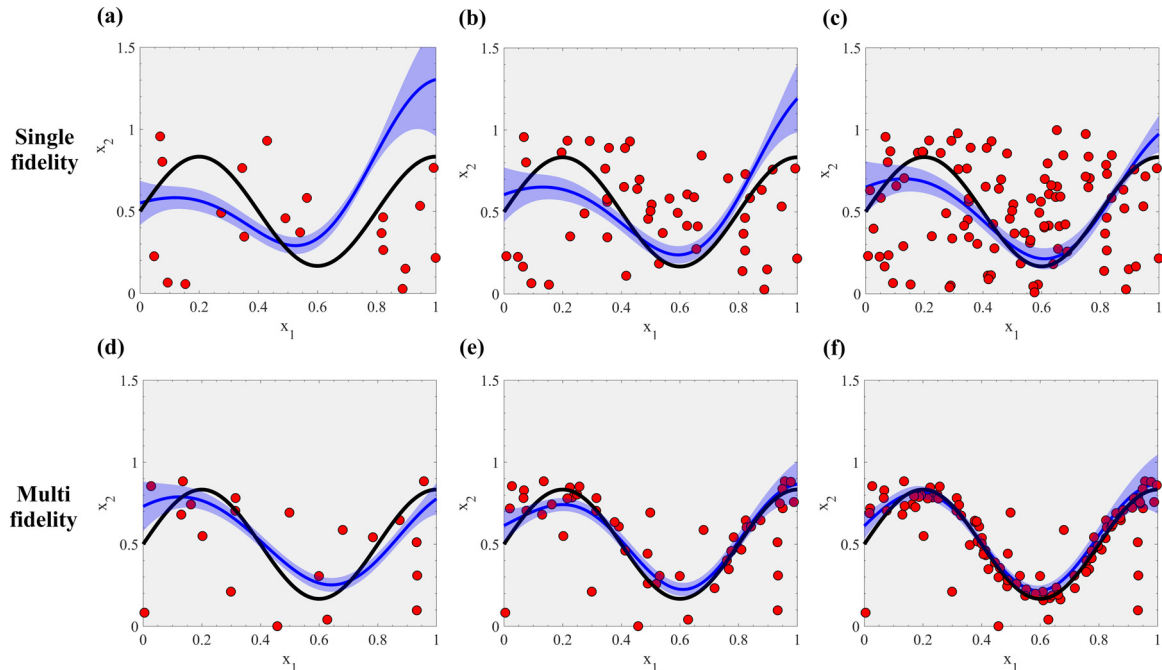


Fig. 2. Boundary estimation results using single and multi fidelity Bayesian classification approaches. True constraint boundary (in black) versus estimated constraint boundary with 95% confidence intervals (in blue). Red dots show where the framework has chosen to query. (a) and (d): 20 queries. (b) and (e): 50 queries. (c) and (f): 100 queries. (For interpretation of the references to color in this figure legend, the reader is referred to the web version of this article.)

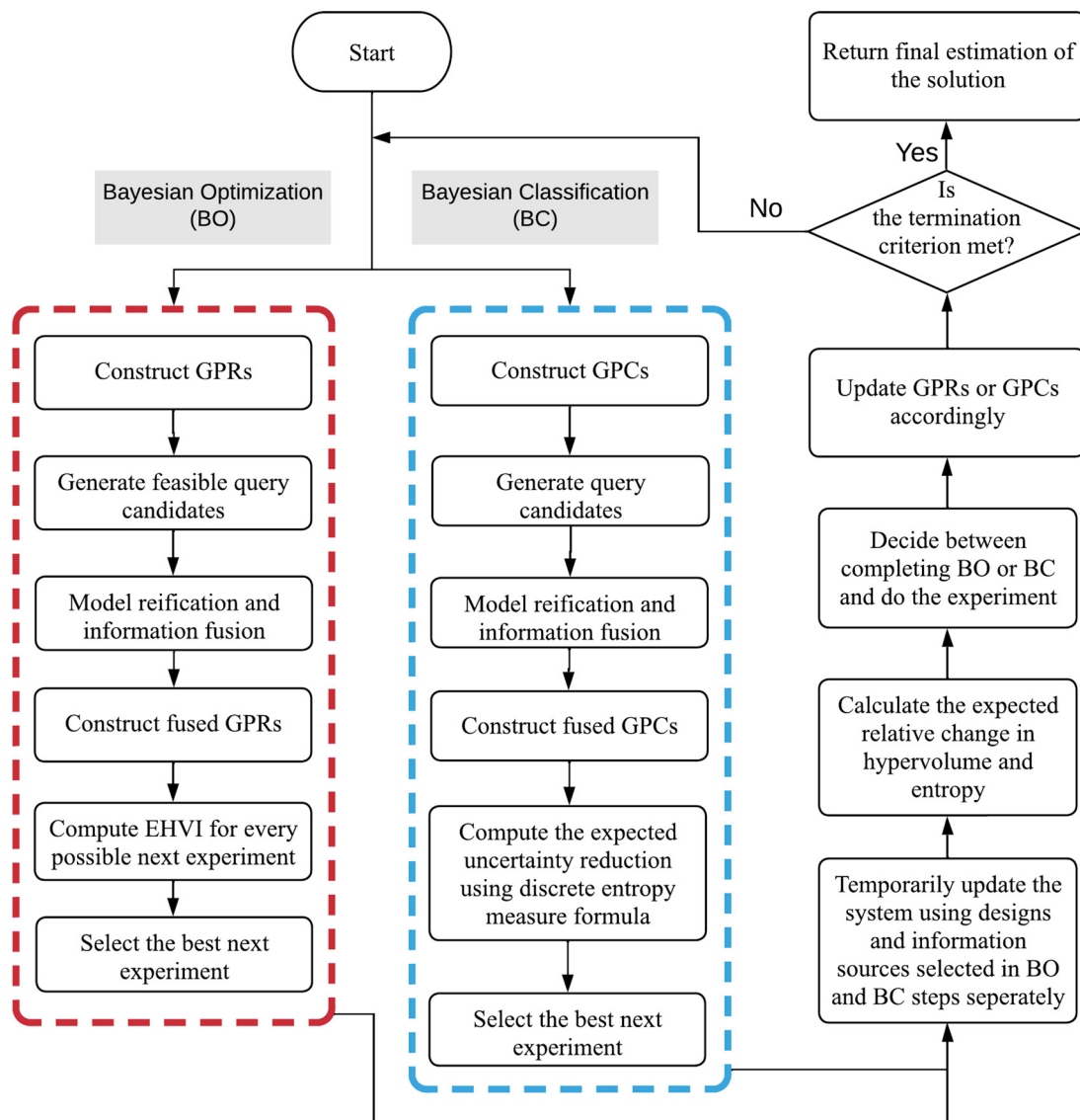


Fig. 3. Flowchart of design framework. This flowchart shows the main steps in the design framework. Gaussian process regressions (GPRs) model the objective function and Gaussian process classifiers (GPCs) model the constraint boundaries.

fore spending any computational resources to test a set of generated samples to search for the best next experiment, fused classifiers determine if all samples are feasible. If not, the unfeasible samples will be removed and new samples are generated until we find the desired number of feasible samples to test. To make decision on feasibility of a design, we used $\mu - 2\sigma > 0.5$ to guarantee at least 95 percent confidence in predictions. One can change this confidence interval accordingly, depending on how hard (or difficult) is a constraint. Then, Expected HyperVolume Improvement (EHVI) is employed as the utility function to search for promising designs to query and increase the hypervolume the most and improve the estimation of the Pareto-front [72].

In the BC component of the framework, to actively learn the constraint boundaries and increase the accuracy of the fused classifiers, an entropy measure is used to gauge the uncertainty in labeling the samples. Since we do binary classification to label samples as either feasible or unfeasible, the problem is reduced to finding the closest samples to the predicted constraint boundary by classifiers. At every iteration of the framework, a decision has to be made between querying the objective functions and thus improving the optimum value of a quantity of interest (hypervolume in

case of multi objective optimization) or querying the constraints and updating classifiers to increase the accuracy of fused classifiers.

To balance the decision between these two options, the expected relative change to the optimum value of an objective (i.e. the expected hypervolume improvement) is calculated and is compared to the relative change in entropy if we update the constraints. This is done by temporarily augmenting the samples determined as the best next experiment and observing the changes in the corresponding values. By comparing the observed relative changes in each case, the framework chooses the action that adds the most value to the system. Note that in both the BO and BC components, multiple information sources may have been employed to represent every objective function and every constraint. Thus, the selected samples are augmented to the GPR or the GPC corresponding to the selected information source.

3.3. Material design process

The design framework depicted in Fig. 3 has been employed to solve the aforementioned alloy design problem. There are two

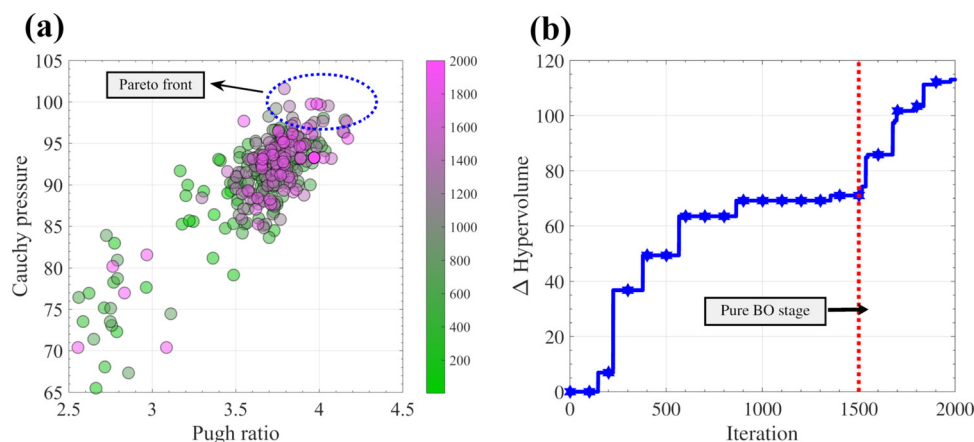


Fig. 4. Final results of introduced material design problem (a) Queried samples from the KKR model in the objective space. Final estimation of the Pareto-front shows 7 non-dominated designs. (b) Improvement in hypervolume of the estimated Pareto-front as a function of iteration. Note that the hypervolume value is depended on the chosen reference point in the objective space, thus, the change in hypervolume is a better indication of making improvements to the Pareto-front estimation.

objectives defined in the problem to be maximized: Pugh's ratio and Cauchy pressure. These objectives encode the intrinsic ductility of candidate alloys. There are two GTE-relevant constraints that must be satisfied: solidus temperature and density of the candidate alloys. The solidus temperature for any composition should be greater than 2000 °C such that the alloy can withstand the hot-zone inside GTEs. Furthermore, the density should be less than 11 g/cm³ such that the alloy is light enough for application in aviation. The design space is 5-dimensional (including temperature). Candidate alloys can consist of permutations and combinations of the following five elements: Mo, Nb, Ti, V, and W. The Thermo-Calc thermodynamic equilibrium model was used as the truth-model that represents the solidus and density constraints. For each constraint, there exists a low order rule-of-mixture approximation. Regarding the objective functions, there are also two models available, one as the lower fidelity information source that is inexpensive to query and responds in a few seconds. Then, a high fidelity KKR model was used as the ground truth (see **Methods** section). Being computationally demanding, the KKR-model was queried after every 10 queries from the lower fidelity information source to update the discrepancy of the low fidelity model and correct its estimation of the objective values.

First remark We would like to note that the design constraints (solidus temperature and density) are relatively easy to estimate using conventional computational thermodynamic techniques. It would thus be possible to simply carry out a high-throughput exploration of the materials space [87] and simply select the feasible region without any active learning step. The purpose of this exercise is to demonstrate the integration of the discovery of the feasible space within a materials optimization framework. This capability would be significant in the case of 'real world' closed-loop materials discovery tasks in which the discovery of the feasible region in a materials design space is highly non-trivial and dependent on exhaustive experimental characterization. For example, the discovery of alloys with acceptable oxidation resistance and optimal mechanical performance may depend on actual experimental oxidation studies. *Our framework is agnostic regarding the nature of the information sources used and thus can easily be adapted to fully experimental or hybrid experimental/computational settings.*

The framework was run over 2000 iterations. Regardless of how much is learned about the constraint boundaries, the last 500 iterations are allocated to perform only optimization to improve the estimated Pareto-front. In later works, an adaptive technique will be taken to increase the weights over optimization than classification as the number of iterations increase.

The results are depicted in Fig. 4. In part (a), queried designs from the KKR model are shown in the objective space and the color map shows the order that queries are made. There are total of 284 queries made from the KKR model, where 229 are made in the last 500 iterations. The final estimation of the Pareto-front consists of 7 non-dominated designs. In Table 1, the design values corresponding to the estimated Pareto-front are specified. In part (b), the change in hypervolume of the estimate Pareto-front as number of iteration is depicted. As the number of iteration increases, the change in hypervolume value gets smaller. Furthermore, it takes more number of iterations to see further improvements in the hypervolume value, however, by allocating the last 500 iteration for optimization purposes, more improvements are made. This essentially shows that as we move toward the final iterations, it is worth to invest on optimization and make the final improvements possible to the solutions. An important point here is that all queried samples are satisfying both solidus temperature and density constraints, which shows how by actively learning the constraint boundaries and using classifiers, querying unfeasible designs is prevented. Tests show that about 20% of the randomly sampled designs violate at least one of the constraints.

Fig. 5 illustrates the cumulative number of actions taken at every iteration. Out of 2000 iterations, 634 iterations are dedicated to perform BO which means 634 queries are made from lower fidelity model. The KKR model is queried in batch of maximum of 5 designs after every 10 queries to the lower fidelity model. To find the batch of designs to be queried from the KKR model, first, a set of query candidates are generated and then their expected hypervolume improvement is calculated. Note that the objective values at every location in the design space are estimated by GPRs that provide normal distributions as the estimation. Then, samples with positive expected hypervolume improvement are kept and clustered by solving a k-medoid problem. Finally, the medoids (i.e. actual points belonging to a cluster in the design space that are maximally separated from other clusters) of these clusters are queried from the KKR model. This approach assures a good distribution of the queried samples all over the space that helps to fully discover the non-dominated region.

Out of 1366 queries from the constraints, 1189 queries are made from the density function. The reason that the framework struggles to identify the density constraint could be the complex shape of feasible and unfeasible regions, making it challenging to recognize the boundary. However, the results show that the framework has learned enough to confidently recognize the feasible regions.

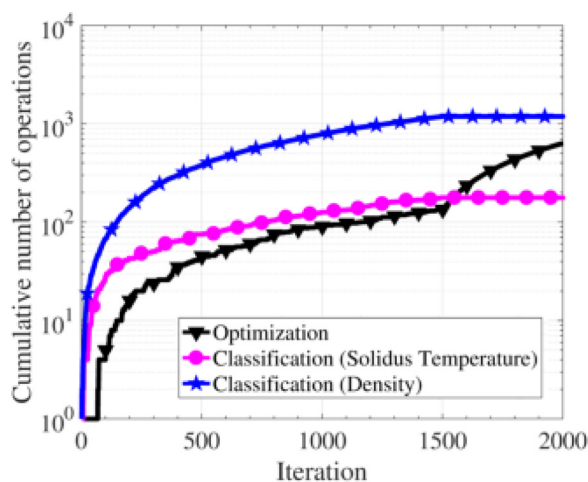


Fig. 5. Cumulative number of operations as a function of iteration. For most number of iterations, the framework has decided to query the density model and update its classifier. It is an indication of the complexity of the density constraint boundary and the framework struggles to learn it and reduce the classifier's uncertainty in labeling the design inputs.

4. Discussion

4.1. HTP brute force analysis to evaluate framework classification

In order to assess the utility of using such a classification framework, we benchmarked the BC of refractory MPEA space against a traditional HTP 'brute-force' approach. In this brute-force approach the density and solidus temperature constraints were queried at increments of 5 at.% considering unary to quinary systems, resulting in 10,626 queries in total. However, with the BC framework, only 1366 queries were needed to find the boundary in the constraint space, dramatically improving the tractability of the problem as the total number of queries over the potentially feasible space was reduced by close to a factor of nine. Querying these expensive information sources is beneficial as it can better elucidate how well the classification aspect of the framework actually performs in this refractory MPEA space.

In order to visualize how composition affects the constrained properties (solidus temperature and density) in this 5-dimensional refractory MPEA space, we rely on a dimensionality reduction technique known as t-distributed stochastic neighbor embedding (tSNE). Each point represents an alloy with a distinct composition. In tSNE embeddings, points that are close to each other in high dimensional space are plotted close to each other in 2-dimensional space. Points colored in Fig. 8c are alloys that contain 50% or more of a particular element. Points closer to the corners of this "pentagonal" shape approach unary compositions. For example, points near the red corner of the tSNE are rich in vanadium; The point on the "corner" represents pure vanadium. Points along the edge connecting the red and blue regions are Mo-V binaries. The inner regions of the tSNE represent the refractory MPEA space. We would like to point out that this representation is mostly qualitative as tSNE embeddings only preserve the local structure of the dataset, while being agnostic with regard to its global structure.

The light blue stars represent the 7 alloys that lie on the Pugh's Ratio-Cauchy Pressure Pareto-front. These alloys are in the Niobium-rich region of the tSNE. Their location in this tSNE embedding provides a visualization of where in the refractory MPEA space the Pareto-front lies. The location of Pareto-front in the refractory MPEA space is not completely unexpected, as Nb has a relatively low VEC of 5. However, according to the prevailing VEC theory of ductility in refractory MPEAs [12], Ti-rich alloys are expected to

be the most ductile in this region as Ti has a VEC of 4, the lowest in the alloy space. However, in Fig. 6a and b, Ti-rich regions have solidus temperatures below 2273 K, violating the solidus constraint. The reason the framework converges on Nb-rich alloys instead of Ti-rich alloys is further demonstrated in Fig. 7 where the property space is plotted. In Fig. 7a the VEC is plotted against the solidus. Many of the Ti-rich alloys (depicted as squares) fall beneath the 2273 K constraint. In Fig. 7b, the Ti-rich alloys that do pass the solidus constraint do not have a large a Pugh's ratio as the Nb-rich alloys (depicted as stars). While not as ductile as Ti-rich alloys, most Nb-rich alloys pass the density and solidus constraints. The classification side of the proposed framework was able to recognize the Ti-rich region of the design space as infeasible by querying the solidus information source only 177 times.

Second remark We would also like to point out that our design setting is truly agnostic with regard to the complexity of the alloy space. Rather than focusing on high-complexity compositions, our framework optimized a set of property targets, subject to application specific design constraints. Whether such compositions are located within the "high entropy" alloy space is immaterial when trying to discover optimal alloys with a target application in mind. It is the view of the authors that property/constraint-aware and "entropy" agnostic exploration of High Entropy Alloy spaces is a more productive research program as compared to approaches that focus on alloy complexity as the sole objective of the alloy design task (Fig. 7).

4.2. DFT analysis of Pareto-front-selected refractory MPEAs

The seven Nb-V rich alloys in Table 1 with superior mechanical properties that comprise the Pareto-front were selected for further analysis using DFT. Singh et al. [88] has shown that the ability of an alloy to resist local distortion and compositional changes have direct impact on ductility. However, the understanding of these features controlling distortion and local compositional changes is currently not discussed well. We performed detailed DFT calculations [74,76,79] of stability (formation energy), distortion factor and local distortion (atomic displacements), and short-range order (local chemical fluctuations) on design compositions.

Generally, refractory materials have very high moduli in the bcc phase because of their low compactness. The interaction between these elements are weaker than other crystal structures such as in fcc materials. Therefore, the ductility is definitely an issue, which helps a material to sustain against permanent (large) deformation under a tensile loading at room temperature without fracturing. In Fig. 8a and b, we plot BM of design compositions with respect to Nb-V composition (in atomic-fraction) and phase stability. The calculated BM was found in the moderate range in Fig. 8a, similar to highly ductile fcc-based materials; moreover, each composition were in the desired MPEA stability range ($-150 \text{ meV-atom}^{-1} < E_{\text{form}} < 65 \text{ meV-atom}^{-1}$) [78].

In Fig. 8c, we plotted distortion metric with respect to scalar displacement, where most compositions show minimal local distortion except #7 that has both large distortion metric and local atomic displacement. Our findings suggest that the distortion factor may further get increased with temperature due to non-uniform local contraction and expansion in different regions with different atomic sizes, which may lead to large thermal strain in local lattices. In Fig. 8d, we found elemental compositions can be tuned to alter local atomic displacement that correlates well with ductility in refractory MPEAs [88]. To provide more detail, we plot distortion metric [88] with respect to difference of VEC (ΔVEC) of bcc alloys in Fig. 8d. The dashed line horizontal to x-axis shows the separation between ductile and brittle materials based on the atomic distortion criterion. Clearly, highly ductile materials are expected to have low distortion as found in fcc alloys.

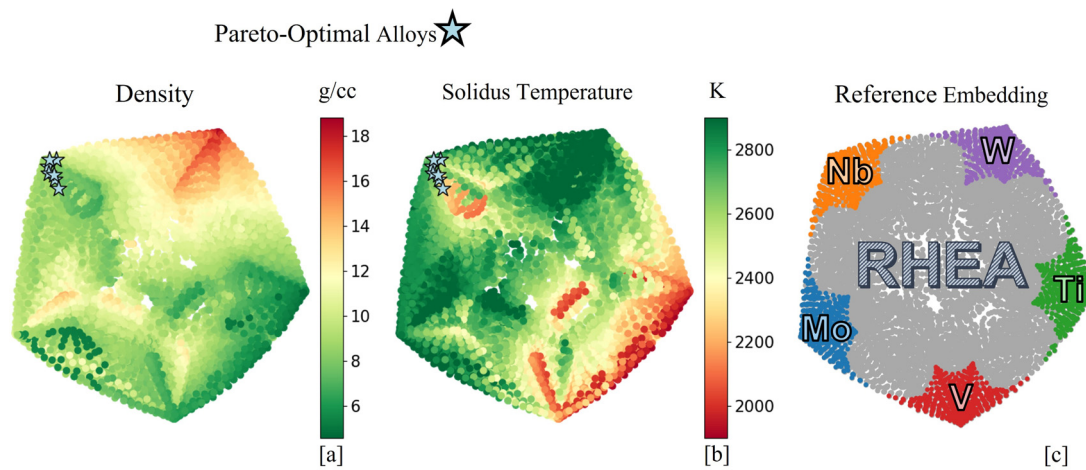


Fig. 6. t-SNE projection of the MoNbTiVW alloy space. Colored points in the reference embedding (right) denote alloys that contain alloys that contain 45% or more of a particular element. The solidus temperature is plotted on the same embedding (right). Likewise, the density is plotted on the embedding (left).

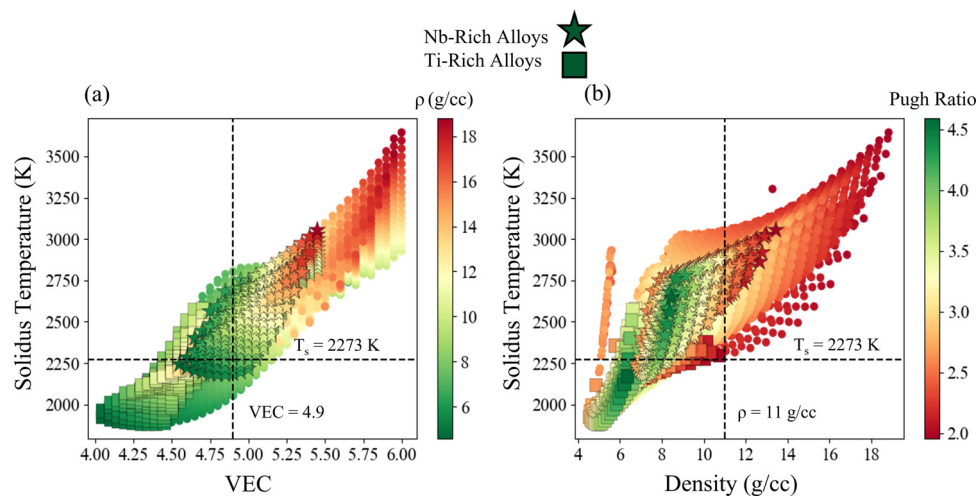


Fig. 7. t-SNE projection of the MoNbTiVW alloy space. Colored points in the reference embedding (right) denote alloys that contain alloys that contain 45% or more of a particular element. The solidus temperature is plotted on the same embedding (right). Likewise, the density is plotted on the embedding (left).

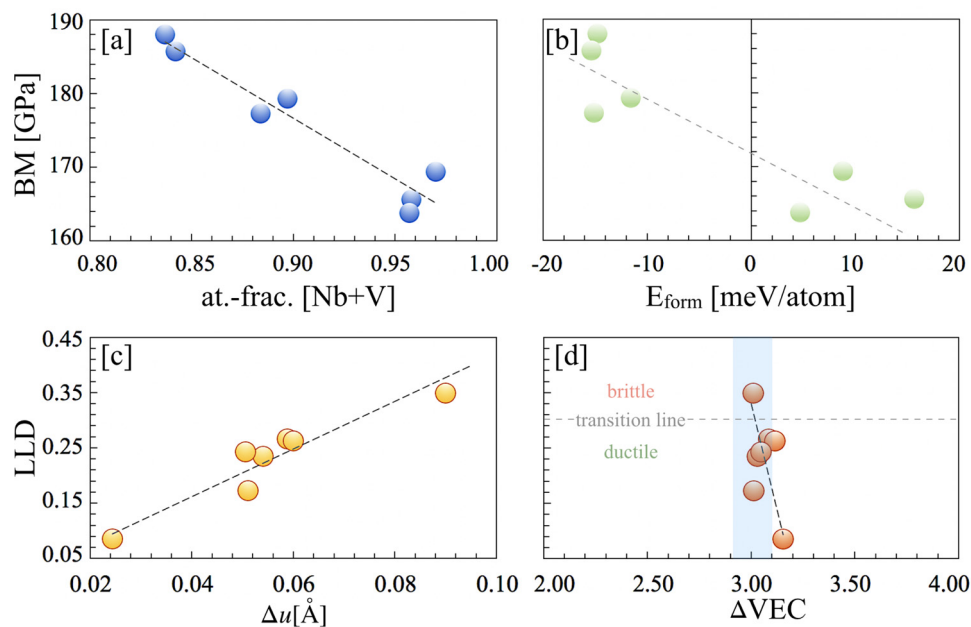


Fig. 8. DFT analysis of thermodynamics and structural properties. (a,b) We plotted bulk-moduli with respect to atomic-fraction (Nb + V) and formation-enthalpy (E_{form}). The structural analysis of key mechanical properties responsible for ductility in Refractory MPEAs, (a) local-lattice distortion with respect to (c) static-displacement, and (d) valence electron count difference in bcc alloys.

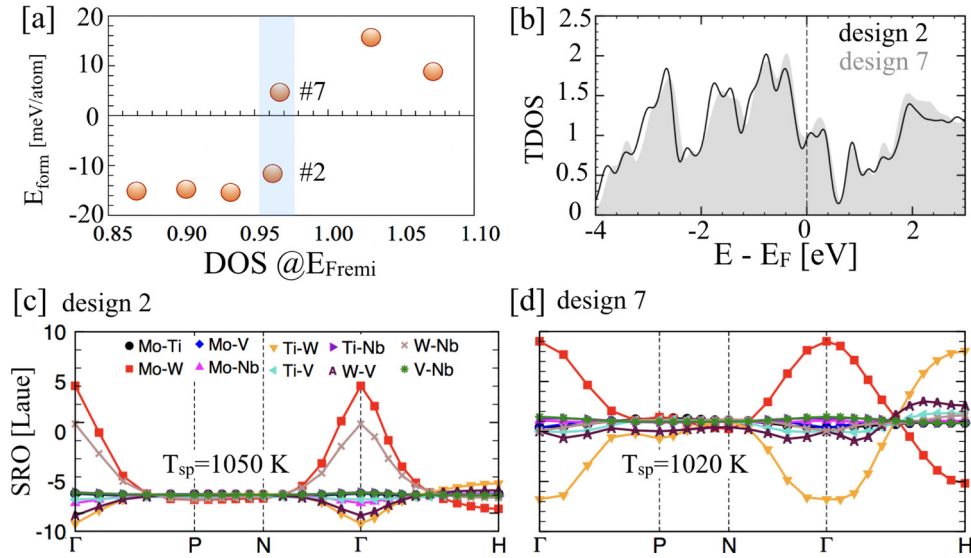


Fig. 9. Electronic-structure and short-range order and analysis. (a) Total DOS at Fermi energy for MPEAs in Table 1. (b) The total density of states (DOS) plot for two key design compositions from the shaded region in (a), i.e., #2 and #7. (c) The total density of states, and (c,d) short-range order for #2 and #7.

Table 1

Non-dominated designs corresponding to the Pareto-front in Fig. 4. Compositions reported in atomic percentage.

Composition elements	Mo	Nb	Ti	V	W
Design 1	0.014	0.738	0	0.233	0.015
Design 2	0.0330	0.8080	0.0090	0.0890	0.0610
Design 3	0.0100	0.7460	0.0050	0.0910	0.1480
Design 4	0.0110	0.6840	0.0150	0.2740	0.0160
Design 5	0.1140	0.7350	0.0010	0.1490	0.0010
Design 6	0.0150	0.8410	0.0550	0.0010	0.0880
Design 7	0.0140	0.7550	0.0160	0.2020	0.0130

Furthermore, defects are very common to refractory alloys, which are detrimental for ductility. Notably, it has been reported that the presence of tungsten up to 5 at.% in refractory-based MPEAs [83] either slows down or stops the formation of new defects, moreover, high-vacancy migration energy of heavier elements also slows down the diffusion of defects. Although our framework was not optimized for defect related properties, the presence of small to moderate at.% molybdenum/tungsten further affirms that new designed compositions in Table 1 satisfy critical feature requirements for ductility. This understanding of low defect concentration in tungsten based alloys can be helpful as the defect creation and propagation into crystal phase make them more fragile at higher strains, which is not desired for high-temperature applications.

The disorder has been shown to induce change in the DOS at/near electronic Fermi energy [89], which can be interpreted as the effect of disorder and electron correlation. The transition-metal-based refractory MPEAs are among the candidate alloys due to the presence of their partially filled *d*-bands. In Fig. 9a, we plot the value of total DOS (TDOS) at the Fermi-level. We found an interesting trend where #2 and #7, despite having the same TDOS values at the Fermi-level, show opposite trends in energy stability. To understand this contrast, we plot total density of states for both the alloys in full energy range (−6 eV to 3 eV). Despite being energetically stable #2 shows an unstable peak at the Fermi-level while #7 shows valley in density of states, and this feature in DOS has been found to correlate well with the alloy stability [90]. But we do not know if this small but finite change in DOS structure at the Fermi-level has any severe impact on thermodynamic behav-

ior or charge fluctuations at finite temperature. The SRO analysis can give us useful information related to local change of chemical compositions, which is a critical aspect of ductile materials.

The local chemical fluctuations [91], if significantly large, may affect the synthesis of single phase alloy and mechanical properties, therefore, we believe understanding change in local response, i.e., short-range behavior (SRO), can give useful guideline regarding minimizing pronounced changes of chemical composition. The SRO theory [76] uses local atomic interaction to predict local chemical behavior, this is important as changes in chemical composition has a strong connection with interaction of alloying elements.

In Fig. 9c and d, we plot the SRO for #2 and #7 MPEAs to reflect on temperature dependent changes in their chemical behavior. Both the alloys in Fig. 9c and d show clustering trend below spinodal temperature (T_{sp}) driven by Mo-W pairs. An absolute instability to k_0 mode [76] occurs below T_{sp} , where $[\alpha^{(-1)}(k_0; T_{\text{sp}})]_{\mu\nu}^{\text{H}} = 0$. For $k_0 = (000)$, the alloy is unstable to segregation (atomic or vacancy clustering), rather than local ordering. Interestingly, we found that the #7 shows competing ordering (B2 ($H = 111$) type) mode while clustering (Γ) mode is slightly stronger, i.e., $\Gamma = (000)$ peak compete with finite k_0 peak. The most unstable SRO mode for both the alloys with large chemical fluctuation has the largest peak in $\alpha_{\mu\nu}(k_0; T > T_{\text{sp}})$ at wavevector k_0 for a specific Mo-W pairs in the solid-solution phase.

The DOS values at Fermi energy for #2 and #7 MPEAs are almost same but their electronic-structure in Fig. 9b at the Fermi energy are quite different, where #2 has small peaks. The finite peak at Fermi energy is the reason for thermodynamic instability towards clustering despite its energy stability ($E_{\text{form}}(\#2) = -12$ meV-atom^{−1}). The prediction of clustering indicates weak interaction among alloying elements both at higher temperature and below T_{sp} , i.e., small or no charge fluctuation in disorder phase.

Except for design composition #7 in Table 1, the DFT analysis indicates the ductility for all other design compositions. The small lattice distortion, weak charge fluctuation, and possibility of low defect concentration in W based alloys [83] of predicted compositions is strong indication that the design framework is able to capture the useful structure-property trend in refractory MPEAs critical for GTEs application.

5. Conclusion

The machinability of refractory MPEAs is a major bottleneck in their development and deployment as structural materials in GTEs. However, with ICME approaches, GTE-amenable refractory MPEAs can be designed with ductility in mind. This can be achieved by optimizing for ductility indicators, such as the Pugh's Ratio and Cauchy Pressure, while under GTE relevant constraints such as the density and the solidus temperature. The Pugh's Ratio and Cauchy Pressure can be estimate with DFT methods; likewise, the density and solidus constraints can be queried by Thermo-Calc's thermodynamic equilibrium simulations, classifying points as feasible based on whether they satisfy both constraints. However, due to the vast nature of the MPEA design space and the high computational cost of these models, computational resources must be allocated in such a way that optimization of objectives is balanced with classification of meeting constraints.

The results from our framework show significant promise in the use of multi-objective and classification frameworks within an ICME methodology for materials design. Most notably, the results showed that the proposed multi-information source BO framework is capable of efficiently exploring high-dimensional materials design spaces under multiple objective targets. Regarding classification, our novel framework (with 1366 queries) is around 8 times faster than the traditional HTP "brute-force" approaches (with 10,626 queries), a huge improvement in terms of resource allocation.

While the proposed framework has been implemented and deployed in an *in silico* platform, the overall principle is truly source-agnostic. Each information source for both objectives and constraints is transformed into a Gaussian Process representation. Therefore, this approach can potentially be deployed for the efficient exploration and exploitation of materials spaces in physical closed-loop materials discovery platforms. With the exponential increase in interest of materials community towards autonomous materials discovery platforms, we believe that the frameworks like one proposed here will provide a useful direction to develop novel material discovery platforms.

Declaration of Competing Interest

The authors declare that they have no known competing financial interests or personal relationships that could have appeared to influence the work reported in this paper.

Acknowledgments

The authors acknowledge the support from the **U.S. Department of Energy** (DOE) ARPA-E ULTIMATE Program through Project **DE-AR0001427**. BV acknowledges the support of **NSF** through Grant no. **DGE-1545403**. DK acknowledges the support of **NSF** through Grant no. **CDSE-2001333**. RA acknowledges the support from Grants no. NSF-CISE-1835690 and NSF-DMREF-2119103. Specific applications of electronic-structure theory at Ames Laboratory were supported by the DOE ARPA-E ULTIMATE Program, while the theory developments at Ames Laboratory were supported by the U.S. DOE, Office of Science, Basic Energy Sciences, Materials Science and Engineering Department. Ames Laboratory is operated by Iowa State University for the U.S. DOE under contract DE-AC02-07CH11358. High-throughput CALPHAD and DFT calculations were carried out in part at the Texas A&M High- Performance Research Computing (HPRC) Facility.

References

- [1] T.M. Pollock, Alloy design for aircraft engines, *Nat. Mater.* 15 (8) (2016) 809–815.

- [2] G. Andrews, 16 - ultra-low nitrogen oxides (NOx) emissions combustion in gas turbine systems, in: P. Jansohn (Ed.), *Modern Gas Turbine Systems*, Woodhead Publishing Series in Energy, Woodhead Publishing, 2013, pp. 715–790, doi:10.1533/9780857096067.3.715. <https://www.sciencedirect.com/science/article/pii/B9781845697280500161>.
- [3] R.C. Reed, *The Superalloys: Fundamentals and Applications*, Cambridge University Press, 2008.
- [4] F.N. Nourin, R.S. Amano, Review of gas turbine internal cooling improvement technology, *J. Energy Resour. Technol.* 143 (8) (2020) 080801, doi:10.1115/1.4048865.
- [5] S. Wee, J. Do, K. Kim, C. Lee, C. Seok, B.-G. Choi, Y. Choi, W. Kim, Review on mechanical thermal properties of superalloys and thermal barrier coating used in gas turbines, *Appl. Sci.* 10 (16) (2020), doi:10.3390/app10165476. <https://www.mdpi.com/2076-3417/10/16/5476>.
- [6] O.N. Senkov, D.B. Miracle, K.J. Chaput, J.P. Couzinie, Development and exploration of refractory high entropy alloys—A review, *J. Mater. Res.* 33 (19) (2018) 3092–3128, doi:10.1557/jmr.2018.153.
- [7] O.N. Senkov, D. Isheim, D.N. Seidman, A.L. Pilchak, Development of a refractory high entropy superalloy, *Entropy* 18 (3) (2016), doi:10.3390/e18030102. <https://www.mdpi.com/1099-4300/18/3/102>.
- [8] U. Bhandari, C. Zhang, S. Yang, Mechanical and thermal properties of low-density $\text{Al}_{20+x}\text{Cr}_{20-x}\text{Mo}_{20-y}\text{Ti}_{20}\text{V}_{20+y}$ alloys, *Crystals* 10 (4) (2020), doi:10.3390/cryst10040278. <https://www.mdpi.com/2073-4352/10/4/278>.
- [9] D. Wang, J. Tan, C. Li, X. Qin, S. Guo, Enhanced creep resistance of $\text{Ti}_{30}\text{Al}_{25}\text{Zr}_{25}\text{Nb}_{20}$ high-entropy alloy at room temperature, *J. Alloys Compd.* 885 (2021) 161038, doi:10.1016/j.jallcom.2021.161038. <https://www.sciencedirect.com/science/article/pii/S0925838821024476>.
- [10] K.-C. Lo, Y.-J. Chang, H. Murakami, J.-W. Yeh, A.C. Yeh, An oxidation resistant refractory high entropy alloy protected by CrTaO_4 -based oxide, *Sci. Rep.* 9 (1) (2019) 1–12.
- [11] N. Philips, M. Carl, N. Cunningham, New opportunities in refractory alloys, *Metall. Mater. Trans. A* 51 (7) (2020) 3299–3310.
- [12] S. Sheikh, S. Shafeie, Q. Hu, J. Ahlström, C. Persson, J. Veselý, J. Zýka, U. Klement, S. Guo, Alloy design for intrinsically ductile refractory high-entropy alloys, *J. Appl. Phys.* 120 (16) (2016) 164902.
- [13] J. Allison, Integrated computational materials engineering: a perspective on progress and future steps, *JOM* 63 (4) (2011) 15–18.
- [14] A. Solomou, G. Zhao, S. Boluki, J.K. Joy, X. Qian, I. Karaman, R. Arróyave, D.C. Lagoudas, Multi-objective Bayesian materials discovery: application on the discovery of precipitation strengthened niti shape memory alloys through micromechanical modeling, *Mater. Des.* 160 (2018) 810–827.
- [15] R.-R. Griffiths, J.M. Hernández-Lobato, Constrained Bayesian optimization for automatic chemical design using variational autoencoders, *Chem. Sci.* 11 (2) (2020) 577–586.
- [16] K.M. Jablonka, G.M. Jothiappan, S. Wang, B. Smit, B. Yoo, Bias free multiobjective active learning for materials design and discovery, *Nat. Commun.* 12 (1) (2021) 1–10.
- [17] L. Qi, D. Chrzan, Tuning ideal tensile strengths and intrinsic ductility of bcc refractory alloys, *Phys. Rev. Lett.* 112 (11) (2014) 115503.
- [18] S.M. Shaikh, V. Hariharan, S.K. Yadav, B. Murty, Calphad and rule-of-mixtures: a comparative study for refractory high entropy alloys, *Intermetallics* 127 (2020) 106926, doi:10.1016/j.intermet.2020.106926. <https://www.sciencedirect.com/science/article/pii/S0966979520305112>.
- [19] L. Chen, X. Zhang, Y. Wang, X. Hao, H. Liu, Microstructure and elastic constants of AlTiVMoNb refractory high-entropy alloy coating on $\text{Ti6Al}_4\text{V}$ by laser cladding, *Mater. Res. Express* 6 (11) (2019) 116571, doi:10.1088/2053-1591/ab49e7. <https://doi.org/10.1088/2053-1591/ab49e7>.
- [20] Y. Ye, B. Musico, Z. Lu, L. Xu, Z. Lei, V. Keppens, H. Xu, T. Nieh, Evaluating elastic properties of a body-centered cubic NbHfZrTi high-entropy alloy—A direct comparison between experiments and ab initio calculations, *Intermetallics* 109 (2019) 167–173, doi:10.1016/j.intermet.2019.04.003. <https://www.sciencedirect.com/science/article/pii/S0966979518311245>.
- [21] S. Pugh, XCII. Relations between the elastic moduli and the plastic properties of polycrystalline pure metals, *London, Edinb., Dublin Philos. Mag. J. Sci.* 45 (367) (1954) 823–843, doi:10.1080/14786440808520496.
- [22] D.G. Pettifor, Theoretical predictions of structure and related properties of intermetallics, *Mater. Sci. Technol.* 8 (4) (1992) 345–349, doi:10.1179/mst.1992.8.4.345.
- [23] D. Khatamsaz, A. Molkeri, R. Couperthwaite, J. James, R. Arróyave, D. Allaire, A. Srivastava, Efficiently exploiting process-structure-property relationships in material design by multi-information source fusion, *Acta Mater.* 206 (2021) 116619.
- [24] D. Khatamsaz, A. Molkeri, R. Couperthwaite, J. James, R. Arróyave, A. Srivastava, D. Allaire, Adaptive active subspace-based efficient multifidelity materials design, *Mater. Des.* 209 (2021) 110001.
- [25] S.F. Ghoreishi, D.L. Allaire, A fusion-based multi-information source optimization approach using knowledge gradient policies, in: 2018 AIAA/ASCE/AHS/ASC Structures, Structural Dynamics, and Materials Conference, 2018, p. 1159.
- [26] S.F. Ghoreishi, A. Molkeri, A. Srivastava, R. Arroyave, D. Allaire, Multi-information source fusion and optimization to realize ICME: application to dual-phase materials, *J. Mech. Des.* 140 (11) (2018) 111409, doi:10.1115/1.4041034.
- [27] S.F. Ghoreishi, D. Allaire, Multi-information source constrained Bayesian optimization, *Struct. Multidiscip. Optim.* 59 (3) (2019) 977–991, doi:10.1007/s00158-018-2115-z.

- [28] D. Khatamsaz, L. Peddareddygar, S. Friedman, D. Allaire, Bayesian optimization of multiobjective functions using multiple information sources, *AIAA J.* 58 (2021) 1–11.
- [29] S. Ghoreishi, W. Thomison, D. Allaire, Sequential information-theoretic and reification-based approach for querying multi-information sources, *J. Aerosp. Inf. Syst.* 16 (12) (2019) 575–587.
- [30] C.E. Rasmussen, C.K.I. Williams, *Gaussian Processes for Machine Learning* (Adaptive Computation and Machine Learning), The MIT Press, 2005.
- [31] F.S. Costabal, P. Perdikaris, E. Kuhl, D.E. Hurtado, Multi-fidelity classification using Gaussian processes: accelerating the prediction of large-scale computational models, *Comput. Methods Appl. Mech. Eng.* 357 (2019) 112602.
- [32] D. Allaire, K. Willcox, Fusing information from multifidelity computer models of physical systems, in: 2012 15th International Conference on Information Fusion, IEEE, 2012, pp. 2458–2465.
- [33] S.F. Ghoreishi, W.D. Thomison, D. Allaire, Sequential information-theoretic and reification-based approach for querying multi-information sources, *J. Aerosp. Inf. Syst.* 16 (12) (2019) 575–587, doi:10.2514/1.1010753.
- [34] W.D. Thomison, D.L. Allaire, A model reification approach to fusing information from multifidelity information sources, in: 19th AIAA Non-Deterministic Approaches Conference, 2017, p. 1949, doi:10.2514/6.2017-1949.
- [35] M. Clyde, Model averaging, Subjective and Objective Bayesian Statistics, second ed., Wiley-Interscience, 2003, doi:10.1002/9780470317105.ch13.
- [36] M. Clyde, E. George, Model uncertainty, *Stat. Sci.* 19 (2004) 81–94, doi:10.1214/088342304000000035.
- [37] D. Draper, Assessment and propagation of model uncertainty, *J. R. Stat. Soc. Ser. B* 57 (1) (1995) 45–97, doi:10.1111/j.2517-6161.1995.tb02015.x.
- [38] J. Hoeting, D. Madigan, A. Raftery, C. Volinsky, Bayesian model averaging: a tutorial, *Stat. Sci.* 14 (4) (1999) 382–417, doi:10.1214/ss/1009212814.
- [39] E. Leamer, Specification Searches: Ad Hoc Inference with Nonexperimental Data, John Wiley & Sons, New York, NY, 1978, doi:10.2307/1057568.
- [40] D. Madigan, A. Raftery, Model selection and accounting for model uncertainty in graphical models using occam's window, *Am. Stat. Assoc.* 89 (428) (1994) 1535–1546, doi:10.1080/01621459.1994.10476894.
- [41] A. Mosleh, K. Apostolakis, The assessment of probability distributions from expert opinions with an application to seismic fragility curves, *Risk Anal.* 6 (4) (1986) 447–461, doi:10.1111/j.1539-6924.1986.tb00957.x.
- [42] J. Reinert, G. Apostolakis, Including model uncertainty in risk-informed decision making, *Ann. Nucl. Energy* 33 (4) (2006) 354–369, doi:10.1016/j.anucene.2005.11.010.
- [43] M. Riley, R. Grandhi, Quantification of modeling uncertainty in aeroelastic analyses, *J. Aircr.* 48 (3) (2011) 866–873, doi:10.2514/1.C031059.
- [44] E. Zio, G. Apostolakis, Two methods for the structured assessment of model uncertainty by experts in performance assessments of radioactive waste repositories, *Reliab. Eng. Syst. Saf.* 54 (2–3) (1996) 225–241, doi:10.1016/S0951-8320(96)00078-6.
- [45] S. Julier, J. Uhlmann, A non-divergent estimation algorithm in the presence of unknown correlations, in: Proceedings of the American Control Conference, 1997, pp. 2369–2373, doi:10.1109/ACC.1997.609105.
- [46] S. Geisser, A Bayes approach for combining correlated estimates, *J. Am. Stat. Assoc.* 60 (1965) 602–607, doi:10.1080/01621459.1965.10480816.
- [47] P. Morris, Combining expert judgments: a Bayesian approach, *Manag. Sci.* 23 (1977) 679–693, doi:10.1287/mnsc.23.7.679.
- [48] R. Winkler, Combining probability distributions from dependent information sources, *Manag. Sci.* 27 (4) (1981) 479–488, doi:10.1287/mnsc.27.4.479.
- [49] N. Alexandrov, R. Lewis, C. Gumbert, L. Green, P. Newman, Approximation and model management in aerodynamic optimization with variable-fidelity models, *AIAA J.* 38 (6) (2001) 1093–1101, doi:10.2514/2.2877.
- [50] D. Allaire, K. Willcox, Surrogate modeling for uncertainty assessment with application to aviation environmental system models, *AIAA J.* 48 (8) (2010) 1791–1803, doi:10.2514/1.1050247.
- [51] V. Balabanov, R. Haftka, B. Grossman, W. Mason, L. Watson, Multifidelity response surface model for HSCT wing bending material weight, 7th AIAA/USAF/NASA/ISSMO Symposium on Multidisciplinary Analysis and Optimization, St. Louis, MO, 1998, doi:10.2514/6.1998-4804.
- [52] V. Balabanov, G. Venter, Multi-fidelity optimization with high-fidelity analysis and low-fidelity gradients, in: 10th AIAA/ISSMO Multidisciplinary Analysis and Optimization Conference, Albany, New York, 2004, doi:10.2514/6.2004-4459.
- [53] S. Choi, J.J. Alonso, L.M. Kroo, Two-level multifidelity design optimization studies for supersonic jets, *J. Aircr.* 46 (3) (2009) 776–790, doi:10.2514/1.34362.
- [54] M. Eldred, A. Giunta, S. Collis, Second-order corrections for surrogate-based optimization with model hierarchies, in: 10th AIAA/ISSMO Multidisciplinary Analysis and Optimization Conference, 2004, doi:10.2514/6.2004-4457.
- [55] A. March, K. Willcox, Convergent multifidelity optimization using Bayesian model calibration, *Struct. Multidiscip. Optim.* 46 (1) (2012) 93–109, doi:10.2514/6.2010-9198.
- [56] A. March, K. Willcox, Provably convergent multifidelity optimization algorithm not requiring high-fidelity derivatives, *AIAA J.* 50 (5) (2012) 1079–1089, doi:10.2514/1.1051125.
- [57] R.L. Winkler, Combining probability distributions from dependent information sources, *Manag. Sci.* 27 (4) (1981) 479–488, doi:10.1287/mnsc.27.4.479.
- [58] D. Khatamsaz, D.L. Allaire, A comparison of reification and cokriging for sequential multi-information source fusion, in: AIAA Scitech 2021 Forum, 2021, p. 1477.
- [59] S.F. Ghoreishi, A. Molkeri, R. Arróyave, D. Allaire, A. Srivastava, Efficient use of multiple information sources in material design, *Acta Mater.* 180 (2019) 260–271.
- [60] S.F. Ghoreishi, S. Friedman, D.L. Allaire, Adaptive dimensionality reduction for fast sequential optimization with Gaussian processes, *J. Mech. Des.* 141 (7) (2019) 1–12, doi:10.1115/1.4043202.
- [61] R.T. Marler, J.S. Arora, The weighted sum method for multi-objective optimization: Pareto front generation, *Struct. Multidiscip. Optim.* 41 (6) (2010) 853–862, doi:10.1007/s00158-009-0460-7.
- [62] I.Y. Kim, O.L. de Weck, Adaptive weighted-sum method for bi-objective optimization: Pareto front generation, *Struct. Multidiscip. Optim.* 29 (2) (2005) 149–158, doi:10.1007/s00158-004-0465-1.
- [63] I. Das, J.E. Dennis, Normal-boundary intersection: a new method for generating the Pareto surface in nonlinear multicriteria optimization problems, *SIAM J. Optim.* 8 (3) (1998) 631–657, doi:10.1137/S1052623496307510.
- [64] N. Beume, S-metric calculation by considering dominated hypervolume as Klee's measure problem, *Evol. Comput.* 17 (4) (2009) 477–492, doi:10.1162/evco.2009.17.4.17402.
- [65] L. Bradstreet, L. While, L. Barone, A fast many-objective hypervolume algorithm using iterated incremental calculations, in: IEEE Congress on Evolutionary Computation, IEEE, 2010, pp. 1–8, doi:10.1109/CEC.2010.5586344.
- [66] M.T. Emmerich, A.H. Deutz, J.W. Klinkenberg, Hypervolume-based expected improvement: monotonicity properties and exact computation, in: 2011 IEEE Congress on Evolutionary Computation (CEC), IEEE, 2011, pp. 2147–2154, doi:10.2514/6.2015-0143.
- [67] C.M. Fonseca, L. Paquete, M. López-Ibáñez, An improved dimension-sweep algorithm for the hypervolume indicator, in: 2006 IEEE International Conference on Evolutionary Computation, IEEE, 2006, pp. 1157–1163, doi:10.1109/CEC.2006.1688440.
- [68] L.M. Russo, A.P. Francisco, Quick hypervolume, *IEEE Trans. Evol. Comput.* 18 (4) (2013) 481–502, doi:10.1109/TEVC.2013.2281525.
- [69] Q. Yang, S. Ding, Novel algorithm to calculate hypervolume indicator of Pareto approximation set, in: International Conference on Intelligent Computing, Springer, 2007, pp. 235–244, doi:10.1007/978-3-540-74282-1_27.
- [70] E. Zitzler, L. Thiele, Multiobjective evolutionary algorithms: a comparative case study and the strength pareto approach, *IEEE Trans. Evol. Comput.* 3 (4) (1999) 257–271, doi:10.1109/4235.797969.
- [71] D. Khatamsaz, L. Peddareddygar, S. Friedman, D.L. Allaire, Efficient multi-information source multiobjective Bayesian optimization, in: AIAA Scitech 2020 Forum, 2020, p. 2127, doi:10.2514/6.2020-2127.
- [72] G. Zhao, R. Arroyave, X. Qian, Fast exact computation of expected hypervolume improvement, 2018.
- [73] A.J. Joshi, F. Porikli, N. Papanikolopoulos, Multi-class active learning for image classification, in: 2009 IEEE Conference on Computer Vision and Pattern Recognition, IEEE, 2009, pp. 2372–2379.
- [74] D.D. Johnson, D.M. Nicholson, F.J. Pinski, B.L. Gyorffy, G.M. Stocks, Density-functional theory for random alloys: total energy within the coherent-potential approximation, *Phys. Rev. Lett.* 56 (1986) 2088–2091, doi:10.1103/PhysRevLett.56.2088. <https://link.aps.org/doi/10.1103/PhysRevLett.56.2088>.
- [75] J.P. Perdew, K. Burke, M. Ernzerhof, Generalized gradient approximation made simple, *Phys. Rev. Lett.* 77 (1996) 3865–3868, doi:10.1103/PhysRevLett.77.3865. <https://link.aps.org/doi/10.1103/PhysRevLett.77.3865>.
- [76] P. Singh, A.V. Smirnov, D.D. Johnson, Atomic short-range order and incipient long-range order in high-entropy alloys, *Phys. Rev. B* 91 (2015) 224204, doi:10.1103/PhysRevB.91.224204. <https://link.aps.org/doi/10.1103/PhysRevB.91.224204>.
- [77] P. Singh, S. Picak, A. Sharma, Y.I. Chumlyakov, R. Arroyave, I. Karaman, D.D. Johnson, Martensitic transformation in $\text{Fe}_{x}\text{Mn}_{80-x}\text{Co}_{10}\text{Cr}_{10}$ high-entropy alloy, *Phys. Rev. Lett.* 127 (2021) 115704, doi:10.1103/PhysRevLett.127.115704.
- [78] P. Singh, A. Sharma, A.V. Smirnov, M.S. Djalilo, P.K. Ray, G. Balasubramanian, D.D. Johnson, Design of high-strength refractory complex solid-solution alloys, *npj Comput. Mater.* 4 (1) (2018) 16, doi:10.1038/s41524-018-0072-0.
- [79] G. Kresse, J. Furthmüller, Efficient iterative schemes for ab initio total-energy calculations using a plane-wave basis set, *Phys. Rev. B* 54 (1996) 11169–11186, doi:10.1103/PhysRevB.54.11169.
- [80] G. Kresse, J. Hafner, Ab initio molecular dynamics for liquid metals, *Phys. Rev. B* 47 (1993) 558–561, doi:10.1103/PhysRevB.47.558.
- [81] G. Kresse, J. Furthmüller, Efficiency of ab-initio total energy calculations for metals and semiconductors using a plane-wave basis set, *Comput. Mater. Sci.* 6 (1) (1996) 15–50, doi:10.1016/0927-0256(96)00008-0. <https://www.sciencedirect.com/science/article/pii/S0927025696000080>.
- [82] R. Singh, A. Sharma, P. Singh, G. Balasubramanian, D.D. Johnson, Accelerating computational modeling and design of high-entropy alloys, *Nat. Comput. Sci.* 1 (1) (2021) 54–61, doi:10.1038/s43588-020-00006-7.
- [83] A. Roy, P. Singh, G. Balasubramanian, D.D. Johnson, Vacancy formation energies and migration barriers in multi-principal element alloys, *Acta Mater.* 226 (2022) 117611, doi:10.1016/j.actamat.2021.117611. <https://www.sciencedirect.com/science/article/pii/S1359645421009897>.
- [84] H.J. Monkhorst, J.D. Pack, Special points for Brillouin-zone integrations, *Phys. Rev. B* 13 (1976) 5188–5192, doi:10.1103/PhysRevB.13.5188.
- [85] G. Kresse, D. Joubert, From ultrasoft pseudopotentials to the projector augmented-wave method, *Phys. Rev. B* 59 (1999) 1758–1775, doi:10.1103/PhysRevB.59.1758.
- [86] P.E. Blochl, Projector augmented-wave method, *Phys. Rev. B* 50 (1994) 17953–17979, doi:10.1103/PhysRevB.50.17953.
- [87] A. Abu-Odeh, E. Galvan, T. Kirk, H. Mao, Q. Chen, P. Mason, R. Malak, R. Arroyave, Efficient exploration of the high entropy alloy composition-phase space, *Acta Mater.* 152 (2018) 41–57.

- [88] P. Singh, R. Arroyave, D. Johnson, A structural signature for ductility in chemically complex alloys, 2022. In review (submitted).
- [89] B. Altshuler, A. Aronov, Zero bias anomaly in tunnel resistance and electron-electron interaction, *Solid State Commun.* 30 (3) (1979) 115–117, doi:[10.1016/0038-1098\(79\)90967-0](https://doi.org/10.1016/0038-1098(79)90967-0). <https://www.sciencedirect.com/science/article/pii/0038109879909670>.
- [90] P. Singh, A.V. Smirnov, D.D. Johnson, Ta-Nb-Mo-W refractory high-entropy alloys: anomalous ordering behavior and its intriguing electronic origin, *Phys. Rev. Mater.* 2 (2018) 055004, doi:[10.1103/PhysRevMaterials.2.055004](https://doi.org/10.1103/PhysRevMaterials.2.055004).
- [91] T. Mukherjee, J.S. Zuback, A. De, T. DebRoy, Printability of alloys for additive manufacturing, *Sci. Rep.* 6 (1) (2016) 19717, doi:[10.1038/srep19717](https://doi.org/10.1038/srep19717).